Available online at www.sciencedirect.com
SCIENCE DIRECT®
International Journal of Solids and Structures 42 (2005) 4574–4587
INTERNATIONAL JOURNAL OF SOLIDS and STRUCTURES
www.elsevier.com/locate/ijsolstr

Elliptic yield cap constitutive modeling for high porosity sandstone

Eric Grueschow *, John W. Rudnicki

Department of Mechanical Engineering, Northwestern University, 2145 Sheridan Rd, Evanston, IL 60208, USA

Received 1 October 2004; received in revised form 1 February 2005
Available online 10 March 2005

Abstract

Field and laboratory investigators have observed thin, tabular zones of localized compressional deformation without shear in high porosity sandstone. These 'compaction bands' display greatly reduced porosity, and may affect the withdrawal of fluids from reservoirs. Studies addressing band formation as a type of strain localization predict the onset of the bands in a range of constitutive parameters roughly consistent with experiments, but are highly dependent on the constitutive relation used. In particular, the hardening modulus in shear and the slope of the yield surface in a plot of shear stress versus mean compressive stress are critical to localization predictions. Previous yield cap constitutive models employed a single deformation criterion, linking hydrostatic and shear response. In this work, we propose an elliptic yield cap model employing separate inelastic deformation parameters along each axis of the ellipse. The two deformation parameters allow the proposed surface to change in aspect ratio as it deforms, and allow a negative hardening modulus in shear without a negative hydrostatic modulus. Some cases with simplified modeling are shown for illustrative purposes, followed by a comparison with existing models. The proposed model displays similar strain behavior to the other models, but predicts localization under less restrictive conditions.

Keywords: Compaction; Constitutive relations; Localization; Geomechanics; Porosity

1. Introduction

Field observations of thin zones of localized compressional deformation without shear have been identified in high porosity sandstones. Mollema and Antonelli (1996) first referred to these structures as 'compaction bands'. Olsson (1999) and Wong et al. (2001) were able to produce bands of localized compaction

* Corresponding author. Tel.: +1 847 467 6279; fax: +1 847 491 3915.
E-mail addresses: e-grueschow@northwestern.edu (E. Grueschow), jwrudn@northwestern.edu (J.W. Rudnicki).

0020-7683/$ - see front matter © 2005 Elsevier Ltd. All rights reserved.
doi:10.1016/j.ijsolstr.2005.02.001

in laboratory sandstone samples. In these samples, the bands were oriented normal to the maximum compressive stress direction. Similar deformation behavior has been observed in other porous materials, including polycarbonate honeycombs (Papka and Kyriakides, 1998) and metallic foams (Park and Nutt, 2001; Bastawros et al., 2000).

In laboratory samples, porosity within the bands was reduced by at least an order of magnitude (Olsson et al., 2002; Klein et al., 2001) and significant grain breakage occurred (DiGiavanni et al., 2000; Baud et al., 2004). Permeability within the band was generally strongly reduced (Holcomb and Olsson, 2003; Vajdova et al., 2004). The reduction in porosity tends to reduce permeability, but grain fracture can create additional fluid pathways (Fortin et al., in press; Zhu and Wong, 1996). Grain breakage within compaction bands may contribute to borehole breakouts (Haimson, 2001, 2003). Thus, compaction bands in reservoirs may affect the withdrawal of fluids or add particulate contaminants.

Olsson (1999) addressed compaction bands as a form of localization following the method of Rudnicki and Rice (1975). Issen and Rudnicki (2000) determined the necessary conditions for the inception of compaction localization without shear along a cap surface. These studies predict the onset of the bands in a range of constitutive parameters roughly consistent with experiments, but the predictions are highly dependent on the constitutive relation used. Constitutive parameters important to the prediction of localization include the plastic hardening modulus in shear, the slope of the yield surface, and the ratio of inelastic volume and shear strains. Materials that exhibit compaction localization can be modeled with a yield surface in *differential stress–mean compressive stress* space similar to that shown in Fig. 1. Analyses predict, consistent with experimental observations, that compaction localization is most likely to occur at high mean stress, when the slope of the yield surface, μ, is negative.

Critical state (Schofield and Wroth, 1968) and yield cap (DiMaggio and Sandler, 1971) models have been commonly used for clays, soils, and high porosity rocks. At high hydrostatic stress, both models display negative slope until the yield envelopes close in a plot of differential stress versus mean compressive stress (see Figs. 2 and 3). In critical state models, the 'cap' is a portion of a single yield surface. One deformation parameter is used to model movement of the entire surface. Yield cap models have been used in conjunction with separate surfaces modeling shear failure, intersecting at a yield corner (DiMaggio and Sandler, 1971; Gu et al., 2001) or arranged to intersect smoothly (Fossum and Fredrich, 2000a). The cap surface is elliptic when viewed in a plot of differential stress versus mean stress. Sliding of the cap surface is modeled using a single deformation parameter. The single deformation parameter for both model types is generally fit to the hydrostatic response of the material. The models have had success predicting strain behavior in axisymmetric compression tests.

Recent tests performed in nontraditional stress paths (Olsson and Holcomb, personal communication) do not fit the single parameter models well. In addition, unless the hydrostatic stress versus volume strain

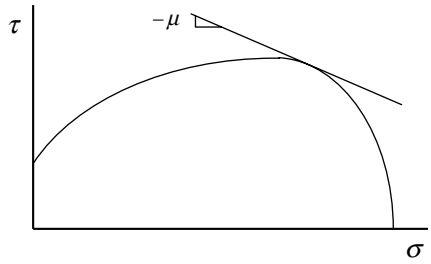

Fig. 1. Representation of a typical yield surface for a material that undergoes compaction localization. The region where the slope of the yield surface, μ, is negative is the 'cap' portion of the yield surface. The yield surface closes across the mean compressive stress axis, so inelastic response is predicted during hydrostatic compression. Compaction localization is usually observed along the lower mean compressive stress portion of this 'cap' surface.

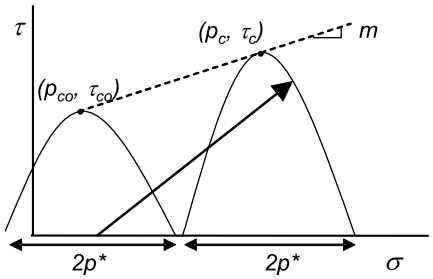

Fig. 2. Layout for the Carroll model in differential stress versus mean stress coordinates. When loaded along the cap region, the peak of the yield surface slides to the right along the critical state line, with slope m. The width, p^*, remains constant. When loading reaches the critical state at the cap peak, the surface remains stationary.

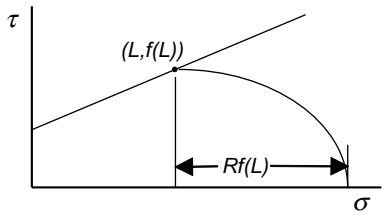

Fig. 3. Layout for the DiMaggio and Sandler model. When loaded along the cap surface, the cap peak moves to the right along the stationary shear surface. The aspect ratio, R, of the elliptical cap remains constant.

response becomes flat, the models are unable to allow a plastic hardening modulus of zero in shear. This prevents the prediction of compaction localization without non-associated flow. A more elaborate constitutive model is needed, with the ability to fit deformation behavior in multiple stress paths and to allow a separate plastic hardening modulus in shear. This new model will help assess whether compaction bands can be accurately predicted as a form of localization using the Rudnicki and Rice method.

This paper introduces a more elaborate cap surface. First, for comparison, a brief description is given for two current models: a critical state model proposed by Carroll (1991) for Boise sandstone and the DiMaggio and Sandler (1971) cap model for McCormick Ranch Sand. After the predicted strain behavior and plastic shear hardening moduli for these models are given for various loading paths, an elliptic quadrant cap surface, with major and minor axes dependent upon separate deformation parameters, is defined. The modeling is similar to that used by Deshpande and Fleck (2000) for metallic foam. The equations are reduced for some simplified cases to show some allowable strain behaviors, including perfectly plastic behavior along either axis. Localization predictions are defined for all three cap surfaces. All the models are compared in an example with a hydrostatic response similar to that displayed by high porosity sandstone.

2. Background

2.1. Carroll model

Carroll (1991) proposed a type of critical state plasticity model using a parabolic yield surface when viewed in differential stress, τ, and mean stress, σ, coordinates. Here, we use the second invariant of the deviatoric stress as the measure of differential stress, defined as $\tau = \sqrt{S_{ij}S_{ij}/2}$, where $S_{ij} = \sigma_{ij} - \delta_{ij}\sigma$. The position of the parabolic vertex (p_c, τ_c) is plastic volume strain dependent and the width, p^*, is held constant

due to micromechanical considerations (see Fig. 2). The vertex moves along the critical state line, with slope m. The yield surface takes the form

$$F_C = 0 = \left(\frac{\sigma - p_c}{p^*}\right)^2 + \frac{\tau}{\tau_c} - 1. \tag{1}$$

If the linear functions used in the original model are generalized, they become

$$\begin{aligned} \tau_c &= \tau_{c0} + mB(\varepsilon_p), \\ p_c &= p_{c0} + B(\varepsilon_p), \end{aligned} \tag{2}$$

where τ_{c0} and p_{c0} are initial values and ε_p is the inelastic volume strain. Because associated flow is assumed, the slope of the yield surface,

$$\mu_c = -\frac{2\tau_c(\sigma - p_c)}{p^{*2}} \tag{3}$$

is equal to the dilatancy factor,

$$\beta = -\mathrm{d}\varepsilon_p/\mathrm{d}\gamma_p, \tag{4}$$

where γ_p is the Mises equivalent shear strain, $\sqrt{2e_{ij}^p e_{ij}^p}$, and $e_{ij}^p = \varepsilon_{ij}^p - (1/3)\delta_{ij}\varepsilon_{kk}^p$.

For stress states with $\sigma > p_c$, the 'cap' portion of the surface, inelastic response is characterized by compactant hardening. The yield surface slides to the right and grows as the vertex moves along the critical state line. Once loading reaches the critical state line, the stress state is fixed at the peak of the parabola. Further inelastic shear strain occurs without inelastic volume strain.

The deformation parameter, B, can be obtained during a hydrostatic test. Because the width of the yield surface is held constant, $\mathrm{d}\sigma = \mathrm{d}p_c$ along the hydrostat. Using the notation $\mathrm{d}\sigma = k_{\mathrm{hydro}}\mathrm{d}\varepsilon_p$ for the hydrostat, where k_{hydro} is the hydrostatic plastic hardening modulus and $k_{\mathrm{hydro}} = B'(\varepsilon_p)$, yields

$$(\mathrm{d}\varepsilon_p)_C = \frac{\mathrm{d}p_c}{k_{\mathrm{hydro}}}. \tag{5}$$

For non-hydrostatic stress paths, where $\mathrm{d}\tau = \alpha\,\mathrm{d}\sigma$, the plastic strain response is determined by applying (2) and (5) to the derivative of (1), resulting in

$$\left(\mathrm{d}\sigma/\mathrm{d}\varepsilon_p\right)_c = k_{\mathrm{hydro}} \frac{2\sqrt{1 - \dfrac{\tau}{\tau_c} + \dfrac{\tau m p^*}{\tau_c^2}}}{2\sqrt{1 - \dfrac{\tau}{\tau_c} + \dfrac{\alpha p^*}{\tau_c}}}. \tag{6}$$

Eq. (6) shows that as the ratio τ/τ_c increases, the plastic strain response decreases from the hydrostatic response, $(\mathrm{d}\sigma/\mathrm{d}\varepsilon_p)_c = k_{\mathrm{hydro}}$ to $(\mathrm{d}\sigma/\mathrm{d}\varepsilon_p)_c = \frac{k_{\mathrm{hydro}} m}{\alpha}$ at the yield surface peak.

The volumetric plastic hardening modulus, k, is important in determining localization predictions, and is defined as

$$k = \mathrm{d}\sigma/\mathrm{d}\varepsilon_p\big|_{\tau=\mathrm{const}}. \tag{7}$$

This volumetric form is more suitable for application on a cap surface than the traditionally used hardening modulus in shear. For the Carroll model, the volumetric plastic hardening modulus is

$$k_c = k_{\mathrm{hydro}}\left(1 + \frac{\tau}{\tau_c}\frac{m}{|\mu_c|}\right). \tag{8}$$

2.2. DiMaggio–Sandler model

DiMaggio and Sandler (1971) proposed a two surface model for McCormick Ranch Sand. The model also has been used for other granular soils and rocks (Fossum and Fredrich, 2000b). The model implements a stationary nonlinear dilatant yield surface at low hydrostatic stress and a hardening elliptic cap surface at high hydrostatic stress (see Fig. 3). The surfaces intersect at the cap peak. If the function defining the dilatant yield surface used in the original model is generalized as $f(L)$, the cap surface takes the form

$$F_{\mathrm{DS}} = 0 = \left(\frac{\sigma - L(\varepsilon_{\mathrm{p}})}{Rf(L)}\right)^2 + \left(\frac{\tau}{f(L)}\right)^2 - 1, \tag{9}$$

where R is the constant aspect ratio of the elliptical surface and $(L,f(L))$ is the point of intersection with the dilatant surface in triaxial stress space. The hydrostatic hardening response determines the movement of L as a function of ε_{p}. During inelastic response, the cap surface slides to the right while maintaining a constant shape. The stress state is assumed to remain constant once loading reaches the dilatant yield surface at the cap peak.

The deformation parameter can be obtained during a hydrostatic test. The aspect ratio is held constant, thus $\mathrm{d}\sigma = \mathrm{d}L(Rf' + 1)$ along the hydrostat, where f' is the slope of the shear surface. Again using the notation $\mathrm{d}\sigma = k_{\mathrm{hydro}}\mathrm{d}\varepsilon_{\mathrm{p}}$ for the hydrostat yields

$$(\mathrm{d}\varepsilon_{\mathrm{p}})_{\mathrm{DS}} = \mathrm{d}L\frac{(Rf' + 1)}{k_{\mathrm{hydro}}}. \tag{10}$$

The plastic strain response to nonhydrostatic stress paths, determined by inserting (10) into the derivative of (9), is

$$\left(\mathrm{d}\sigma/\mathrm{d}\varepsilon_{\mathrm{p}}\right)_{\mathrm{DS}} = \frac{k_{\mathrm{hydro}}}{Rf' + 1}\left(\frac{\sqrt{1 - \left(\frac{\tau}{f}\right)^2} + Rf'}{\sqrt{1 - \left(\frac{\tau}{f}\right)^2} + \alpha R\frac{\tau}{f}}\right). \tag{11}$$

As the ratio τ/f in (11) increases from zero, the plastic strain response decreases from the hydrostatic response to $(\mathrm{d}\sigma/\mathrm{d}\varepsilon_{\mathrm{p}})_{\mathrm{DS}} = \frac{k_{\mathrm{hydro}}f'}{\alpha(Rf'+1)}$ as it reaches the cap peak. The volumetric plastic hardening modulus is

$$k_{\mathrm{DS}} = \frac{k_{\mathrm{hydro}}}{Rf' + 1}\left(1 + \frac{f}{\tau}\frac{f'}{|\mu_{\mathrm{DS}}|}\right), \tag{12}$$

where

$$\mu_{\mathrm{DS}} = -\frac{(\sigma - L)}{\tau R^2}. \tag{13}$$

Associated flow is assumed for this model as well.

The parabolic surface for the Carroll Model remains at a constant width and varies in height, allowing a straightforward fit to hydrostatic data, whereas the elliptic surface of the DiMaggio–Sandler model has a more complex hydrostatic fit and constant yield surface shape. A minimum of four tests are needed to define the DiMaggio–Sandler model. At least two low confining pressure axisymmetric compression tests are needed to locate the dilatant shear surface, which we take to correspond with the critical state line of the Carroll model. A hydrostatic test is needed to locate the initial yield surface and to define the surface evolution, and one additional high confining pressure axisymmetric compression test is needed to define the

elliptical shape of the cap surface. The Carroll model requires three tests to define the initial shape and location of the yield surface, the surface evolution, and the critical state line.

3. Constitutive modeling of new surface

The cap surface is modeled as an ellipse quadrant with axes at $\sigma = \sigma_0$ and $\tau = 0$ (see Fig. 4), and takes the form

$$F = 0 = \left(\frac{\tau}{a}\right)^2 + \left(\frac{\sigma - \sigma_0}{b}\right)^2 - 1, \tag{14}$$

with

$$\begin{aligned} a &= a(\gamma_p), \\ b &= b(\varepsilon_p). \end{aligned} \tag{15}$$

Parameters a and b define the size of the yield ellipse, and increase with inelastic shear strain and inelastic volume strain, respectively. Another yield surface is needed to model behavior below σ_0. A similar elliptical surface without an intersecting shear surface was defined by Deshpande and Fleck (2000) for metallic foams, with $\sigma_0 = 0$ and parameters a and b as linear functions of both measures of plastic strain. By using (4) and (15) and taking the derivative of (14), we can determine

$$d\gamma_p = \frac{(\alpha - \mu)\, d\sigma}{\left(\frac{\tau}{a}\right) da/d\gamma_p + \mu\beta\left(\frac{\sigma - \sigma_0}{b}\right) db/d\varepsilon_p}, \tag{16}$$

where the substitution

$$\mu = -\frac{(\sigma - \sigma_0)a^2}{\tau b^2} \tag{17}$$

is used. Associated flow is not necessary for modeling, but for nonassociated flow, a definition is needed for β. This modeling can be used for any loading path.

3.1. Determining model parameters

A minimum of three tests are needed to define the model. A hydrostatic test is used to find the initial hydrostatic yield stress, b_0, and to fit the relation $k_{hydro} = db/d\varepsilon_p$. Two additional tests are needed to locate

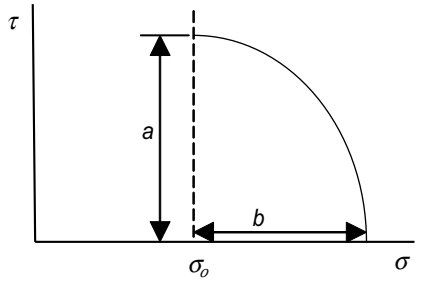

Fig. 4. Ellipse model layout in differential stress versus mean compressive stress coordinates. The model is centered at $(\sigma_0, 0)$. The vertical axis length, a, is a function of inelastic shear strain, and the horizontal axis length, b, is a function of inelastic volume strain.

σ_0 and the initial condition a_0 and to define a relation $\mathrm{d}a/\mathrm{d}\gamma_\mathrm{p}$. For other cap models, the shear and cap surfaces are often assumed to intersect at the cap peak (e.g. DiMaggio–Sandler model), but this is not necessary. If the surfaces do not intersect at the cap peak, however, determination of σ_0 and a_0 may be difficult.

The relation $\mathrm{d}a/\mathrm{d}\gamma_\mathrm{p}$ is determined most easily with a constant mean stress test, where the confining pressure is reduced properly as the axial load is increased, allowing an increase in differential stress without a change in mean stress. This loading direction gives a direct measure of the traditionally used plastic hardening modulus in shear, h_ELL, and (16) can be simplified for this case as

$$\frac{\mathrm{d}\tau}{\mathrm{d}\gamma_\mathrm{p}} = \left(\frac{\tau}{a}\right)\mathrm{d}a/\mathrm{d}\gamma_\mathrm{p} + \mu\beta\left(\frac{\sigma-\sigma_0}{b}\right)k_\mathrm{hydro} = h_\mathrm{ELL} \tag{18}$$

and fit to the data curve. The volumetric plastic hardening modulus is

$$k_\mathrm{ELL} = \left(\frac{\sigma-\sigma_0}{b}\right)k_\mathrm{hydro} + \left(\frac{1}{\mu\beta}\right)\left(\frac{\tau}{a}\right)\mathrm{d}a/\mathrm{d}\gamma_\mathrm{p}. \tag{19}$$

The hardening modulus for this model, unlike (8) and (12), can decrease to zero without applying $k_\mathrm{hydro} = 0$. This is valuable, because softening in shear, correlating with $\mathrm{d}a/\mathrm{d}\gamma_\mathrm{p} < 0$, may be reasonable for high porosity sandstones, but hydrostatic softening is not generally observed.

To help display the capabilities of the model, some special cases will be considered. First, linear plastic flow along each axis is discussed. Perfectly plastic behavior along either axis is also considered.

3.2. Linear plastic flow

If we assume a linear hardening law along each axis of the form

$$\begin{aligned} \mathrm{d}a &= C_1\,\mathrm{d}\gamma_\mathrm{p}, \\ \mathrm{d}b &= C_2\,\mathrm{d}\varepsilon_\mathrm{p}, \end{aligned} \tag{20}$$

Eqs. (4) and (16) simplify to

$$\begin{aligned} \mathrm{d}a &= \frac{(\alpha-\mu)\,\mathrm{d}\sigma}{\dfrac{\tau}{a} + c\mu\beta\dfrac{\sigma-\sigma_0}{b}}, \\ \beta &= -\frac{1}{c}\,\mathrm{d}b/\mathrm{d}a, \end{aligned} \tag{21}$$

where the substitution

$$c = C_2/C_1 \tag{22}$$

is used. Parameter c gives a hardening ratio between the linear flow laws. Cases where either axis is stationary, corresponding to a hardening ratio of zero or infinity, are considered in the next section.

Fig. 5 shows the evolution of the yield surface for different stress paths beginning at σ_0. For the plots shown, $R_0 = 1$ and $c = 1$. All final yield surfaces occur after the same amount of radial loading from σ_0. The endpoints each have a different final yield surface, due to path dependency. Isotropic hardening occurs along $\alpha = 1$. Loading along the paths $\alpha \to \infty$, the constant mean stress path at σ_0, and $\alpha = 0$, the hydrostat, result in surface movement along the nearest axis only. The increase in a is greater along the path $\alpha = \sqrt{3}$, corresponding to a standard axisymmetric compression test, than either the isotropic loading path or the

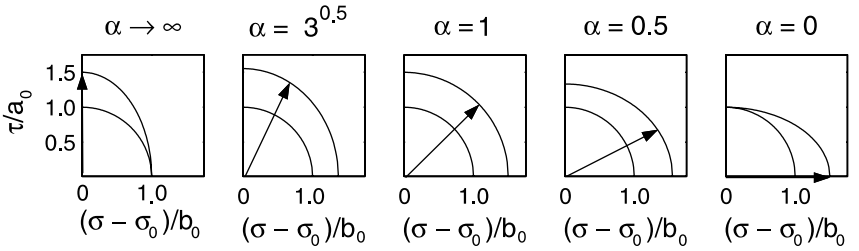

Fig. 5. Evolution of the ellipse model yield surface during loading in different stress directions from the ellipse center, σ_0. Note that the $\alpha = 1$ sample displays isotropic hardening, and that the final length a is greater for the standard axisymmetric stress path $\alpha = \sqrt{3}$ than the path along the axis or the isotropic direction. For these plots, $a_0 = b_0$ and $c = 1$.

path along the axis. This results in greater inelastic shear strain for the axisymmetric test than the other tests.

3.3. Perfectly plastic hydrostatic behavior

If a material displays plastic hardening much more readily in shear than hydrostatically, equivalent to a hardening ratio near zero, the parameter b can be modeled as perfectly plastic, or constant. Because only one deformation parameter is active, all points with the same inelastic shear strain will lie along the same yield surface. In addition, differing positive loading paths reaching the same point in stress space will lie along the same yield surface. The dilatancy factors at this point in the tests will be equal, but the ratio of accumulated inelastic strains will not.

Fig. 6 shows the response for samples loaded along axisymmetric compression paths starting at different hydrostatic stresses. Fig. 6a shows the evolution of the yield surface in *differential stress–mean compressive stress* coordinates. The endpoints were selected to lie along the same yield surface. The mean compressive stress versus inelastic volume strain response is shown in Fig. 6b. The inelastic shear strains are equal at the endpoints. Tests at higher confining pressures display a flatter response and require larger inelastic volume strains to reach the final surface.

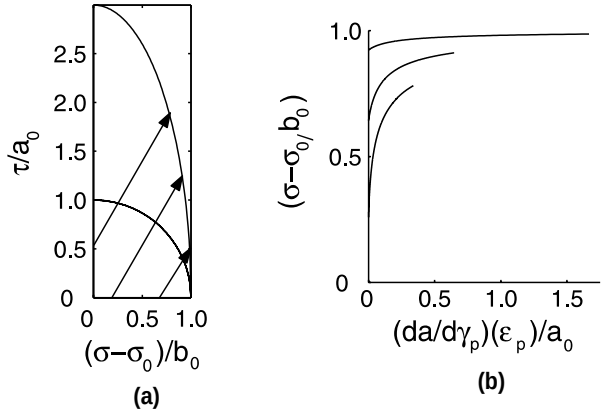

Fig. 6. Ellipse model behavior when only the vertical axis deforms. Plots are normalized by the size of the initial yield surface and magnitude of the shear parameter $\mathrm{d}a/\mathrm{d}\gamma_p$. For these plots, $a_0 = b_0$. (a) Evolution of the yield surface for standard axisymmetric compression tests. All endpoints lie on the same yield surface. (b) Mean stress versus inelastic volume strain behavior. All tests have the same final inelastic shear strain, but different inelastic volume strains.

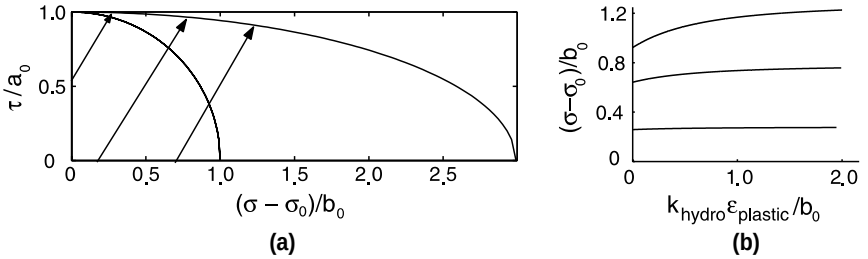

Fig. 7. Ellipse model behavior when only the horizontal axis deforms. Plots are normalized by the size of the initial yield surface and the magnitude of the hydrostatic parameter k_{hydro}. For these plots, $a_0 = b_0$. (a) Evolution of the yield surface for standard axisymmetric compression tests. All endpoints lie on the same yield surface. (b) Mean stress versus inelastic volume strain behavior. Note that all tests have the same final inelastic volume strain.

3.4. Perfectly plastic shear behavior

If a material displays much more plastic hardening hydrostatically than in shear, equivalent to a nearly infinite hardening ratio, parameter a can be modeled as constant. Fig. 7 shows the modeled behavior for loading along axisymmetric compression paths starting at different hydrostatic stresses. Fig. 7a shows the evolution of the yield surface, with all tests ending along the same final yield surface. As can be seen in Fig. 7b, the inelastic volume strains are equal at the endpoints. Tests at lower confining pressures display a flatter response.

4. Localization along cap surface

Strain localization is an allowable bifurcation from uniform flow when the hardening modulus falls below the critical value for a band orientation. The critical volumetric plastic hardening modulus for compaction localization along a surface, but not at the intersection of surfaces, is (Rudnicki, 2004)

$$\frac{k_{\text{cr}}}{G} = \frac{1+\upsilon}{9(1-\upsilon)}\left[\left(\sqrt{\frac{\mu}{\beta}} - \sqrt{\frac{\beta}{\mu}}\right)^2 - \left(\sqrt{\frac{3}{\mu\beta}} + \left(\sqrt{\frac{\mu}{\beta}} + \sqrt{\frac{\beta}{\mu}}\right)\right)^2\right] \tag{23}$$

when simplified for axisymmetric loading. This result can also be obtained from the plastic hardening modulus in shear given by Issen and Rudnicki (2000) with the substitution $h_{\text{cr}} = \mu\beta k_{\text{cr}}$. Behavior at the intersection of yield surfaces is more complex (Issen, 2002; Challa and Issen, 2004), and is not considered here. Once the hardening modulus decreases to the critical value, compaction localization is expected.

Shear bands have a different critical hardening modulus. The orientation with the highest critical value is expected to occur first. If localization occurs, compaction bands are the predicted orientation if

$$\mu + \beta < -\sqrt{3}. \tag{24}$$

Otherwise, for cases along a cap surface, shear localization is the predicted orientation.

Associated flow is often assumed along cap surfaces, but nonassociated flow may be applicable away from the hydrostatic axis. Both the DiMaggio–Sandler and the Carroll models employ associated flow, but nonassociated flow of the form

$$\beta = A\mu, \tag{25}$$

where A is a positive constant, could be inserted without problem. Flow of this form still allows a critical state approach at the yield surface peak, as $\mu = \beta = 0$ at the peak. We assume flow of the form (25), where $A = 1$ for associated flow. Using this form, relation Eq. (24) can be simplified to the form

$$\mu < \frac{-\sqrt{3}}{1+A} \tag{26}$$

for compaction bands. Considering Eqs. (4), (13), and (17), compaction localization is predicted over a greater portion of the cap if the ratio of the cap height to cap width is larger. If the volumetric plastic hardening modulus goes to zero, compaction localization is predicted only when the critical hardening modulus is above zero. From (23) and (25), this occurs when

$$-\frac{\sqrt{3}}{2} < \mu < -\frac{\sqrt{3}}{2A} \tag{27}$$

and $A > 1$. If $0 < A < 1$, the above inequalities are reversed. Considering (26) and (27), the criteria for compaction localization can be defined as

$$-\frac{\sqrt{3}}{2} < \mu < -\frac{\sqrt{3}}{A+1} \tag{28}$$

for $A > 1$, as shown in Fig. 8, and

$$-\frac{\sqrt{3}}{2A} < \mu < -\frac{\sqrt{3}}{A+1} \tag{29}$$

for $0 < A < 1$.

For associated flow, the maximum critical hardening modulus is zero at $\mu = -\sqrt{3}/2$. Considering Eqs. (8) and (12), the Carroll and DiMaggio–Sandler models can only predict localization when $k_{\text{hydro}} = 0$. Experimental results for high porosity sandstone show compaction localization when the hydrostatic modulus is small, but greater than zero (Wong et al., 2001). As shown in (19), the new elliptic surface allows a negative or zero plastic hardening modulus with a positive k_{hydro} and a softening response in shear. Softening in shear may be applicable in high porosity sandstones.

For the proposed model, as seen in Fig. 6a, a stronger hardening response in shear results in a steeper yield surface, and a steeper yield surface predicts compaction localization over a greater portion of the cap. At the same time, a hardening response in shear is resistant to localization. A complex shear response, with initial hardening followed by shear softening, would best meet localization criteria over a large portion of the cap.

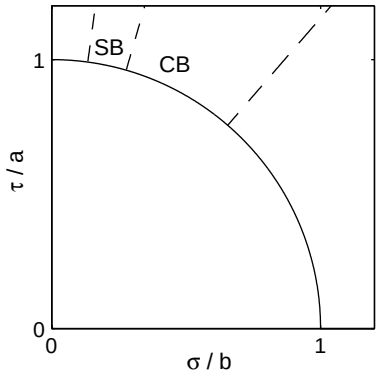

Fig. 8. Regions predicting shear bands (SB) and compaction bands (CB) for perfectly plastic behavior on an elliptical surface with an aspect ratio of one and $A = 5$.

5. Model comparison

An example with more realistic hydrostatic behavior will be used to compare the models. Fig. 9 shows a hydrostatic curve similar to the experimental response of Adamswiller sandstone (Wong and Baud, 1999). Behavior is modeled as elastic until σ_1, and the hydrostatic plastic hardening modulus follows the form

$$k_{\text{hydro}} = B(\varepsilon_{\text{p}} - \varepsilon_{\text{p}}^{0})^2 + C\varepsilon_{\text{p}}. \tag{30}$$

Using reasonable values for material constants (see Table 1), the plastic hydrostatic response was put into the Carroll and DiMaggio–Sandler models. The models were used to predict the response for a set of axisymmetric compression tests at differing confining pressures, and were run until loading reached the cap peak. Figs. 10a and 11a show the mean stress versus total volume strain response for each of the axisymmetric tests, along with the hydrostatic response. Each test displays 'shear assisted compaction' (Wong et al., 2001). For the Carroll model, tests at lower confining stresses display a steeper slope during early plastic strain. For the DiMaggio–Sandler model, tests at higher confining pressures display a steeper slope during early plastic strain. The Carroll model curves are significantly steeper than the DiMaggio–Sandler model curves for all samples. Both models predict stiffening at large plastic strains. If we compare these results to the experimental results for Adamswiller sandstone, loading reaches the peak of the Carroll model at a smaller total strain than was observed for the low confining stress sample. Loading reaches the peak of the DiMaggio–Sandler model at a similar strain to observed failure. All the other samples failed without stiffening. The flatter curves at low confining stress and flatter overall axisymmetric response of the DiMaggio–Sandler model make it a better fit for this set of sandstone data. Plots of the volumetric plastic

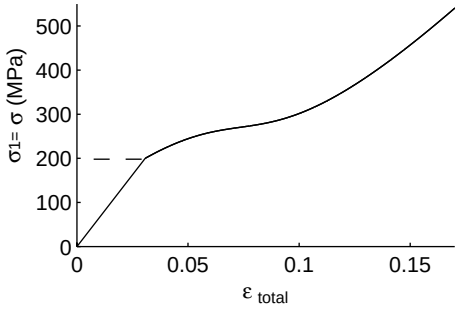

Fig. 9. Hydrostatic response approximation. Elastic response is predicted until $\sigma_1 = 200$ MPa. After a period of weak inelastic response, the material stiffens.

Table 1
Material constants used in Figs. 10–12, elastic bulk modulus: 6500 MPa

Property	Carroll model	DiMaggio–Sandler model	Ellipse model
Initial location of yield surface (MPa)	p_{c0} 75	L_0 75	σ_0 75
Initial height of yield surface (MPa)	τ_{c0} 72.2	f_0 72.2	b_0 72.2
Initial width of yield surface (MPa)	p^* 125	R (width = R^*f) 1.73	a_0 125
Slope of shear surface	m 0.87	f' 0.87	N/A

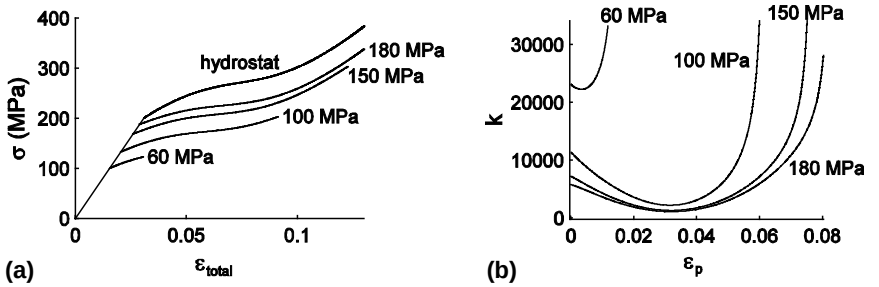

Fig. 10. Predicted response for axisymmetric compression tests at the given confining pressures using the Carroll model. (a) Mean stress–volumetric compressive strain response. The top curve is the hydrostatic response. (b) Plastic hardening modulus at each confining pressure.

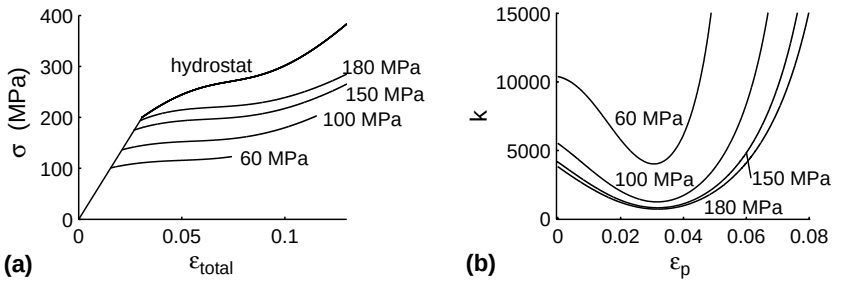

Fig. 11. Predicted response for axisymmetric compression tests at the given confining pressures using the DiMaggio and Sandler model. (a) Mean stress–volumetric compressive strain response. The top curve is the hydrostatic response. (b) Plastic hardening modulus at each confining pressure.

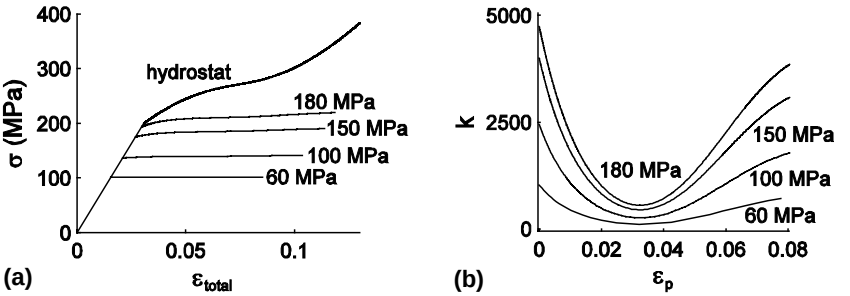

Fig. 12. Predicted response for axisymmetric compression tests at the given confining pressures using the ellipse quadrant model. (a) Mean stress–volumetric compressive strain response. The top curve is the hydrostatic response. (b) Plastic hardening modulus at each confining pressure.

hardening moduli for both models are shown in Figs. 10b and 11b. Because the hardening moduli (8) and (12) depend on (30), the moduli reach a minimum when k_{hydro} is small. Both models predict lower volumetric hardening moduli at the higher confining stresses.

For the ellipse quadrant model, using the same hydrostatic fit (30), assuming associated flow, and holding parameter a stationary fits the data well. As can be seen in Fig. 12a, the initial slopes of the axisymmetric curves at high confining stress are slightly flatter than those of the DiMaggio–Sandler model. The curves

are steeper at higher confining pressures and are relatively flat, similar to the experimental results for Adamswiller sandstone. Stiffening at large plastic strains, predicted by the other models but not observed, is not predicted.

The volumetric plastic hardening modulus for the ellipse model (see Fig. 12b) is less than that of the DiMaggio–Sandler Model by an order of magnitude at the minima. A lower hardening modulus is predicted at lower confining stresses, unlike in the other models. This shows better agreement with the observation that localization usually occurs at intermediate confining pressures (Holcomb and Olsson, 2003). A more complex response for parameter a, with softening at large plastic strains, could be applied, and would yield a hardening modulus below zero. Axisymmetric tests with the mean stress held constant would help to properly constrain parameter a.

6. Conclusions

The proposed yield surface can accommodate complex deformation behavior. Previous models employed a single deformation criterion, allowing the yield surface to expand, translate, or expand and translate at a fixed ratio. With two yield parameters, the proposed surface can change in aspect ratio as it deforms. Non-associated flow is allowed, leaving the plastic strain ratio unrestricted.

In the simplified cases examined, one of the axes displays much greater hardening than the other. This reduces the model to a single deformation criterion. In this case, different positive loading paths to the same point in stress space would lie along the same yield surface. In cases where two deformation parameters are active, loading along different paths will result in different yield surfaces and different accumulations of plastic strain.

Both compaction and shear localization can be predicted along regions of the elliptic cap. Associated flow restricts localization, but localization is predicted at $\mu = -\sqrt{3}/2$ when the hardening modulus is below zero. With increasing non-normality, both compaction bands and shear bands are predicted in growing regions extending further up the cap. Non-normality also allows localization when the hardening modulus is positive.

The aspect ratio of an elliptic yield surface is critical to localization predictions. Steep cap surfaces predict compaction localization over a greater portion of the cap. A vertical flat cap would predict compaction bands as the preferred orientation along the entire cap. Published observations of localization behavior for high porosity sandstones generally display compaction localization on cap areas near the transition between shear localization and compaction localization predictions. A constitutive model that allows the cap to become steeper under continued loading may better predict the localization mode.

The new model allows the plastic hardening modulus to become zero or negative without a flat hydrostatic response. Previous models employing only one inelastic deformation parameter required a flat hydrostatic response, which is not observed in experiments. This feature allows the prediction of compaction localization without requiring nonassociated flow. Tests in nontraditional stress paths would help to better constrain the hardening modulus.

Acknowledgments

The authors thank David Holcomb and Bill Olsson for many stimulating discussions and for their generosity in allowing us to examine their triaxial test data for Castlegate sandstone. Partial financial support for this work was provided by the US Department of Energy, Office of Basic Energy Science, Geosciences Research Program through grant DE-FG-02-93ER14344 to Northwestern University.

References

Bastawros, A.F., Bart-Smith, H., Evans, A.G., 2000. Experimental analysis of deformation mechanisms in a closed-cell aluminum alloy foam. J. Mech. Phys. Solids 48 (2), 301–322.

Baud, P., Klein, E., Wong, T.F., 2004. Compaction localization in porous sandstones: spatial evolution of damage and acoustic emission activity. J. Struct. Geol. 26 (4), 603–624.

Carroll, M.M., 1991. A critical state plasticity theory for porous reservoir rock. Am. Soc. Mech. Eng. 117, Book G00617-1991.

Challa, V., Issen, K.A., 2004. Conditions for compaction band formation in porous rock using a two yield surface model. J. Eng. Mech. Div., Am. Soc. Civ. Eng. 130 (9), 1089–1097.

Deshpande, V.S., Fleck, N.A., 2000. Isotropic constitutive models for metallic foams. J. Mech. Phys. Solids 48 (6–7), 1253–1283.

DiGiavanni, A.A., Fredrich, J.T., Holcomb, D.J., Olsson, W.A., 2000. Micromechanics of compaction in an analogue reservoir sandstone. Proc. 4th North Am. Rock Mech. Symp., pp. 1153–1160.

DiMaggio, F.L., Sandler, I.S., 1971. Material model for granular soils. J. Eng. Mech. Div., Am. Soc. Civ. Eng. 97, 935–950.

Fortin, J., Schubnel, A., Gueguen, Y., in press. Elastic wave velocities and permeability evolution during compaction of Bleuswiller sandstone. Int. J. Rock Mech.

Fossum, A.F., Fredrich, J.T., 2000a. Cap plasticity models and compactive and dilatant pre-failure deformation. Pacific Rocks 2000, Proceedings of the 4th North American Rock Mechanics Symposium. A.A. Balkema, Rotterdam, pp. 1169–1176.

Fossum, A.F., Fredrich, J.T., 2000b. Constitutive models for the Etchegoin sands, Belridge diatomite, and overburden formations at the Lost Hills oil field, CA. Sandia Report, SAND2000-0827.

Gu, C., Kim, M., Anand, L., 2001. Constitutive equations for metal powders: application to powder forming processes. Int. J. Plast. 17, 147–209.

Haimson, B.C., 2001. Fracture-like borehole breakouts in high-porosity sandstone: are they caused by compaction bands? Phys. Chem. Earth A 26 (1–2), 15–20.

Haimson, B.C., 2003. Borehole breakouts in Berea sandstone reveal a new fracture mechanism. Pure Appl. Geophys. 160 (5–6), 813–831.

Holcomb, D.J., Olsson, W.A., 2003. Compaction localization and fluid flow. J. Geophys. Res. 108 (B6), Art. No. 2290.

Issen, K.A., 2002. The influence of constitutive models on localization conditions for porous rock. Eng. Fract. Mech. 69 (17), 1891–1906.

Issen, K.A., Rudnicki, J.W., 2000. Conditions for compaction bands in porous rock. J. Geophys. Res. 105 (B9), 21529–21536.

Klein E, Baud, P., Reuschle, T., Wong, T.F., 2001. Mechanical behaviour and failure mode of Bentheim sandstone under triaxial compression. Phys. Chem. Earth A 26 (1–2), 21–25.

Mollema, P.N., Antonelli, M.A., 1996. Compaction bands: a structural analog for anti-mode I cracks in Aeolian sandstone. Tectonophysics 267, 209–228.

Olsson, W.A., 1999. Theoretical and experimental investigation of compaction bands. J. Geophys. Res. 104, 7219–7228.

Olsson, W.A., Holcomb, D.J., Rudnicki, J.W., 2002. Compaction localization in porous sandstone: implications for reservoir mechanics. Oil Gas Sci. Technol. 57 (5), 591–599.

Papka, S.D., Kyriakides, S., 1998. In-plane crushing of a polycarbonate honeycomb. Int. J. Solids Struct. 35 (3–4), 239–267.

Park, C., Nutt, S.R., 2001. Anisotropy and strain localization in steel foam. Mater. Sci. Eng. A 299 (1–2), 68–74.

Rudnicki, J.W., Rice, J.R., 1975. Conditions for the localization of deformation in pressure-sensitive dilatant materials. J. Mech. Phys. Solids 23, 371–394.

Rudnicki, J.W., 2004. Shear and compaction band formation on an elliptic yield cap. J. Geophys. Res. 109, Art. No. B03402.

Schofield, A., Wroth, C.P., 1968. Critical State Soil Mechanics. McGraw-Hill, New York.

Vajdova, V., Baud, P., Wong, T.F., 2004. Compaction, dilatancy, and failure in porous carbonate rocks. J. Geophys. Res. 109 (B5), Art. No. B05204.

Wong, T.F., Baud, P., Klein, E., 2001. Localized failure modes in a compactant porous rock. Geophys. Res. Lett. 28 (13), 2521–2524.

Wong, T.F., Baud, P., 1999. Mechanical compaction of porous sandstone. Oil Gas Sci. Technol. 54 (6), 715–727.

Zhu, W.L., Wong, T.F., 1996. Permeability reduction in a dilating rock: network modeling of damage and tortuosity. Geophys. Res. Lett. 23 (22), 3099–3102.